
PREF: Phasorial Embedding Fields for Compact Neural Representations

Binbin Huang

Xinhao Yan

Anpei Chen

Shenghua Gao*

Jingyi Yu*

ShanghaiTech University

<https://github.com/hbb1/PREF>

Abstract

We present a phasorial embedding field *PREF* as a compact representation to facilitate neural signal modeling and reconstruction tasks. Pure multi-layer perceptron (MLP) based neural techniques are biased towards low frequency signals and have relied on deep layers or Fourier encoding to avoid losing details. *PREF* instead employs a compact and physically explainable encoding field based on the phasor formulation of the Fourier embedding space. We conduct comprehensive experiments to demonstrate the advantages of *PREF* over the latest spatial embedding techniques. We then develop a highly efficient frequency learning framework using an approximated inverse Fourier transform scheme for *PREF* along with a novel Parseval regularizer. Extensive experiments show our efficient and compact frequency-based neural signal processing technique is on par with and even better than the state-of-the-art in 2D image completion, 3D SDF surface regression, and 5D radiance field reconstruction.

1 Introduction

Coordinate-based neural representations have emerged as a compelling alternative for modeling and processing signals (e.g., sound, image, video, geometry, etc.). Instead of using discrete primitives such as pixels or vertices, coordinate-based multi-layer perceptrons (MLPs) represent graphics images [31, 15, 11], shapes [1, 13, 30, 39], or even radiance fields [8, 23, 29, 32, 34, 38, 58] in terms of continuous functions that are memory efficient and amenable for solving inverse reconstruction problems via training. Earlier coordinate-based MLPs tend to be biased towards low frequencies, whereas more recent implicit neural approaches have adopted a sinusoidal representation for better recovering high frequencies, by either transforming the input coordinates to the Fourier basis [32, 59, 57], or encoding the sinusoidal nonlinearity via deeper MLP architectures [43, 11].

Although effective in countering high frequency losses, such approaches are inefficient in training or inference, inherent to the MLP-based optimization strategy: brute-force mappings from low-dimension, low-frequency inputs onto high frequency target functions do not sufficiently consider the underlying characteristics of the mapping function. As a result, they have largely resorted to large MLPs (either wide in hidden dimensions or deep in layers) to reliably learn the corresponding function mapping. The downside of large MLPs is the long training time and slow inference speed.

To accelerate training, embedding-based MLPs [55, 45, 34, 7] have adopted an inverse optimization strategy. They jointly search for an optimal mapping network and the optimal inputs (i.e., the high dimension embedding volume). By replacing the input field with a high-dimension high-frequency embedding volume (whose size is generally determined by the volume resolution and kernel size), they manage to bridge the gap between the low-dimension low-frequency coordinate inputs and

*Corresponding authors.

the high-frequency outputs with a much smaller MLP in both width and depth. Successes of these approaches are illustrated by their accelerations by orders of magnitudes in both training and rendering [7, 34, 45, 55, 56].

However, as their embedding space is also represented in discrete forms, state-of-the-art techniques have relied on interpolations for querying high-dimensional embedded features. To maintain high efficiency, the most adopted schemes are ubiquitous local interpolation - only a subset of parameters respond to a single position evaluation. Yet they present several major limitations:

- From the optimization perspective, due to the local interpolation, the volume is sparsely updated at query locations during back-propagation, which may result in noises and hinder the overall performance.
- The highest recoverable frequency of the embedding fields is determined by the resolution of the volume. To preserve high frequencies, it is critical to discretize the volume at a very fine level. Fully frequency preservation hence requires demand extremely high memory consumption, prohibitive on even the most advanced GPUs.
- Spatially discretized embedding, compared to its frequency dual, provides limited insights on the signal. In particular, despite a large variety of Fourier signal processing tools for both editing and stylization, few are directly applicable to spatial embedding.

To address these limitations, we present PREF, a novel PhasoRial Embedding Field, that represents the Fourier transformed embedding with compact, complex-numbered phasors. We derive a comprehensive framework using PREF to approximate the Fourier embedding space so that each spatial coordinate’s feature can be represented in terms of the sinusoidal features within a discrete phasor volume. PREF presents several key advantages over previous spatial embedding techniques. First, PREF, as a global representation where each position is synthesised with all spatial supports, avoids producing outliers as opposite to dense volume [55, 45]. Second, PREF is highly compact and does not require using high resolution volumes to preserve high frequency. In fact, it facilitates easy queries of the specific frequency of the input embedding. Finally, based on Fourier transforms, PREF manages to exploit many existing Fourier signal processing techniques such as differentiation, convolution, and Parseval’s theorem to conduct traditionally expensive operations for the spatial counterparts. Overall, PREF provides a new embedding that benefits direct and inverse neural reconstructions on tasks ranging from 2D image completion to 3D point cloud processing and the 5D neural radiance field reconstruction.

To summarize, the contributions of our work include:

- A compact and physically explainable encoding field based on the phasor formulation called PREF. We conduct comprehensive experiments and demonstrate the advantages of PREF over previous spatial embedding techniques.
- We show that PREF provides a robust and compact solution to MLP-based signal processing. It is compact and at the same time effectively preserves high frequency components and therefore details in signal reconstruction.
- We develop a highly efficient frequency learning framework using an approximated inverse Fourier transform scheme along with a novel Parseval regularizer. Comprehensive experiments demonstrate that PREF is on the state-of-the-art techniques in various signal reconstruction tasks in both accuracy and robustness.

2 Related Work

Our PREF framework is in line with renewed interest in adopting implicit neural networks to represent continuous signals from low dimensional input. In computer vision and graphics, they include 2D images with pixels [10], 3D surfaces in the form of occupancy fields [30, 35, 39] or signed distance fields (SDFs) [1, 13, 48, 54, 27, 46, 53, 49], concrete 3D volumes with a density field [17, 40], 4D light fields [21, 50] and 5D plenoptic functions for the radiance fields [32, 58, 36, 25, 38, 54].

Frequency encoding. To learn high frequencies, state-of-the-art implicit neural networks have adopted the Fourier encoding scheme by transforming the coordinates by periodic $\sin(x)$ and $\cos(x)$ functions or equivalently, under Euler’s formula e^{ix} . Under Fourier encoding [47, 59, 32], feature

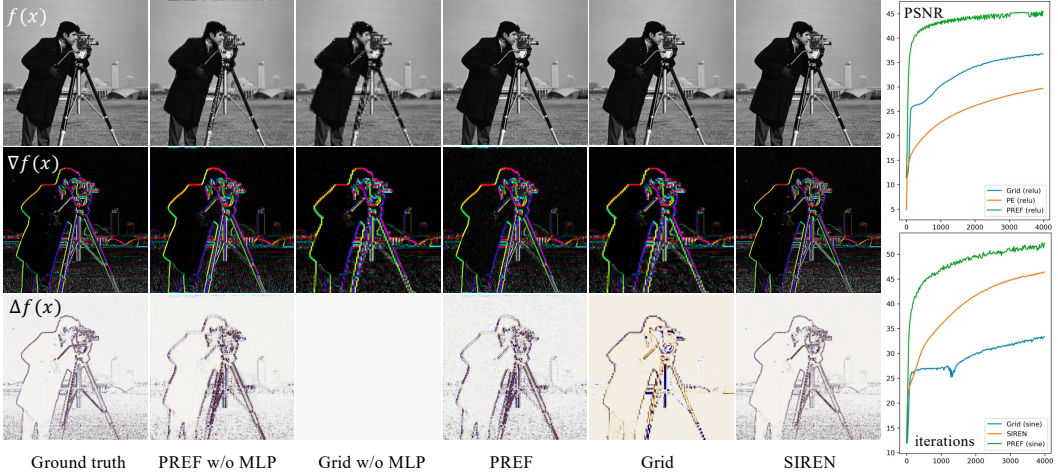


Figure 1: Comparison of spatial encoding and frequency encoding fitting a ground truth image (top left). We show that PREF fits the image well, correctly reflecting its first- and second-order derivatives. On the right plot, we show that PREF consistently outperforms explicit (grid) representation and state-of-the-art implicit neural networks under different activations.

optimization through MLPs can be mapped to optimizing complex-valued matrices with complex-valued inputs in the linear layer, which we call phasor embedding layer. Specifically, Position Encoding (PE) and Fourier Feature Maps (FFM) both transform spatial coordinates to Fourier basis at earlier input layers [32, 47, 59] whereas SIREN [43] and MFN [11] embeds the process in the deeper layers by using periodic activation functions. Accessing frequency representations has also led to many other advances. Frequency encoding schemes allow level-of-detail smoothing and multi-scale anti-aliasing rendering of neural fields [24, 3]. Like Fourier methods [2, 22], frequency-based MLP also supports infinite derivatives that well fit general bounded-value problems [43]. Theoretically, our embedding method inherits these merits and achieves significant acceleration with FFT.

Spatial embedding. Improving the training and inference efficiency of MLP-based networks has also been explored from the embedding perspective with smart data structures. Various schemes [41, 14, 56, 55, 45, 34, 7] replace the deep MLP architecture with voxel-based representations, to trade memory for speed. Early approaches bake an MLP to an Octree along with a kilo sub-NeRF or 3D texture atlas for real-time rendering [41, 14]. These approaches rely on a pre-trained or half-trained MLP as prior and therefore still incur long per-scene training. Plenoxel [55] and DVGO [45] directly optimize the density values on discretized voxels and employ an auxiliary shading function represented by either spherical harmonics (SH) or a shallow MLP network to account for view dependency. They achieve orders of magnitude acceleration over the original NeRF on training but incur a very large memory footprint by storing per-voxel features. However, over parametrization can easily lead to noisy density estimation and subsequently inaccurate surface estimations and rendering. The seminal work of Instant-NGP [34] spatially groups features via embedding with a hash table to achieve unprecedentedly fast training and very visual results. In a similar vein, TensoRF [9] employs highly efficient tensor decomposition via vertical projections. While TensoRF decomposes higher dimension volume into lower dimension volumes via tensor decomposition, we instead use a set of sinusoids with tailored frequencies to comprise the signal. Remarkably, such Fourier-based decomposition serves as a general compression technique that can operate on one dimension data as opposite to Tensor decomposition [9] that applies to higher dimension volume.

Generative latent embedding. It is worth noting that embedding-based techniques share many similarities to neural inversion [16] that aims to jointly optimize the inputs and network weights. In a nutshell, different from traditional feed-forward neural network optimization that attempts to refine network weights, neural inversion seeks to find inputs, often non-unique, that will produce the desired output response under the fixed set of weights. Classic examples include latent embedding optimization [42] in machine learning and GAN inversions [19, 51, 18, 19] that finds the optimal latent code to best match the target image for subsequent editing or stylization. While generative models optimize a semantic latent embedding space that generates datasets, our PREF seeks to represent a frequency latent embedding that matches the dataset, *e.g.*, a collection of posed images.

3 Background and Notations

Our goal is to fit a continuous function $\Phi(\mathbf{x})$ parameterized with low dimensional inputs $\mathbf{x} \in \mathbb{R}^n$. Let $\mathcal{M}(\cdot; \theta)$ be an MLP with parameter θ , $\mathbf{P} \in \mathbb{C}^{k \times N^d}$ be a complex-valued (phasor) volume of dimensionality $n + 1$. $\tilde{\mathcal{T}}$ represents the inverse Fourier Transform. We use the MLP to approximate as $\Phi(\mathbf{x})$ as $\mathcal{M}(f(\mathbf{x}); \theta)$, where $f(\mathbf{x}) \in \mathbb{R}^k$ can be computed as $f(\mathbf{x}) = \tilde{\mathcal{T}}(\mathbf{P}; \mathbf{x})$.

Our phasorial embedding field (PREF) resembles existing spatial embedding. However, spatial embedding uses a real-valued volume rather than a complex-valued volume and employs local interpolation or hash functions in place for $\tilde{\mathcal{T}}$. Similar to spatial embedding though, PREF can also handle any continuous fields by the spatially-embedded MLPs, e.g., signed distance fields (SDFs) [46, 48, 54] or radiance fields (RFs) [9, 45, 55, 32]. In fact, as a frequency-based alternative, PREF explicitly associates frequencies with features: each volume entry represents the Fourier coefficients under the corresponding frequency.

Next, we show that under PREF, many neat properties of the Fourier transform translate to the complex phasor volume, facilitating much more efficient optimization and accessible manipulation. For simplicity, we carry out our derivations in 2D while high dimensional extensions can be similarly derived as shown in various applications.

We first present the inverse Fourier transform, and along the way, present the associate theorems, which we utilize to optimize our phasorial representation. Before proceeding, we explain our notation. Let $F(\cdot)$, $F[\cdot]$ be the continue and discrete Fourier series, and \mathbf{P} is a phasor volume that translates to phasorial embedding field $f(\mathbf{x})$.

Inverse Fourier Transform. Let $f(x, y)$ be a 2D continuous band-limited signal, its discrete inverse Fourier transform $\tilde{\mathcal{T}}$ factorizes the signal into a Fourier series $u \in \mathbb{N}, v \in \mathbb{N}$ with corresponding coefficients:

$$f(x, y) = \tilde{\mathcal{T}}(F) = \sum_{u=0}^{M-1} \sum_{v=0}^{N-1} F[u, v] e^{j2\pi(u \frac{x}{M} + v \frac{y}{N})} \quad (1)$$

Recall that $F[u, v] \in \mathbb{R}^{M \times N}$ corresponds to an equally-spaced matrix where each entry is a phasor with the real and imaginary parts of the corresponding frequency as:

$$F[u, v] = F_R[u, v] + jF_I[u, v] \quad (2)$$

The resulting phasor volume \mathbf{P} can be viewed as a multi-channel version of the Fourier map F . Therefore, \mathbf{P} inherits several nice properties of the Fourier transform, which is efficient for frequency-domain manipulations [5].

Theorem 1. *Let $F(u, v)$ be an absolutely continuous differentiable function, and $f(x, y)$ be its inverse Fourier transform, we have*

$$\frac{\partial f^n(x, y)}{\partial x^n} = \tilde{\mathcal{T}}((j2\pi u)^n F[u, v]) \quad (3)$$

Theorem 2. *Let $F(u, v)$ be absolutely continuous differentiable function, and $f(x, y)$ be its inverse Fourier transform, we have*

$$\iint \|f(x, y)\|^2 dx dy = \sum_{u=0}^{M-1} \sum_{v=0}^{N-1} \|F(u, v)\|^2. \quad (4)$$

Beyond these, modeling a signal in a Fourier domain provides various unique properties; for example, the convolution theorem indicates that a convolution of two spatial signals can be implemented as simple multiplication in the frequency domain.

A naïve solution is to represent the signals based on the standard inverse Fourier transform and a dense phasorial volume grid describing the Fourier coefficients, then jointly update the volume grid and MLP with gradient descent. However, such a solution is inefficient since both model size and computation increase in $\mathcal{O}(N^3)$, where N is the resolution of the Fourier series. We next introduce a novel modeling, phasorial encoding field, for resolving the limitation in the naïve solution.

4 Phasorial Embedding Fields

Our PREF is a de facto continuous feature field $f(x)$ transformed from a multi-channel multi-dimensional Fourier (phasor) volume \mathbf{P} (e.g., $\mathbb{C}^{k \times N^2}$ for 2D tasks). In a nutshell, PREF employs the Fourier transform in Eq. 1 to map spatial coordinate x into k -channel feature $f(x) \in \mathbb{R}^k$. The mapped results can be fed into an MLP to process task-specific fields $\Phi(x)$ such as SDFs or RFs. Fig. 2 illustrate this. As each channel is independent, PREF can transform the spatial coordinates and update the phasor volume in parallel. Therefore, we simply omit k in the rest of the derivations for clarity. We start by defining a phasor volume of PREF and subsequently discuss how to efficiently extract features from PREF and then optimize the volume.

4.1 Dilated Phasor Volume

To preserve high frequencies, spatial embedders require discretizing the volume at a very fine level. By contrast, frequency modeling manages to query specific frequencies without resorting to large volume and memory. To that end, we instead use a tiny volume and dilate it to a large volume with certain frequencies skipped, following [32, 59]. This dilation process is equivalent to selectively marking a large portion of the entries in the full matrix $F(u, v)$ as zero. In particular, we set out to factorize $\mathbf{P}[u, v] \in \mathbb{C}^{N \times N}$ by logarithmic sampling along each dimension. This results in two thin matrices $\mathbf{P}^u = \mathbf{P}[u, k] \in \mathbb{C}^{N \times D}$, $k = [0, 1, 2, \dots, 2^{D-2}]$ and $\mathbf{P}^v = \mathbf{P}[l, v] \in \mathbb{C}^{D \times N}$, $l = [0, 1, 2, \dots, 2^{D-2}]$, with D being a small number. Consequently, such a transform simplifies to $f(x, y) = \tilde{\mathcal{T}}(\mathbf{P}^v) + \tilde{\mathcal{T}}(\mathbf{P}^u)$. The formulations can be also extended to a higher dimensional signal with a similar dilation along individual dimensions. It is also noteworthy that if the length of non-dilated dimensions equals 1, i.e., only a few on-axis dilated frequencies comprise the support, then PREF degenerates to PE [32].

Recall recovering $f(x, y)$ corresponds to transforming the *dilated phasor volume* - a full volume $\mathbf{P}[u, v]$ with selectively marking specific entries as zero along each dimension. For clarity, we use the same notation of full volume $\mathbf{P}[u, v]$ from Sec. 4.2 and to 4.3. A more detailed discussion on complexity is carried out in Sec. 4.4.

4.2 Inverse Fourier Transform Approximation

As opposite to explicit (spatial) schemes where a single position in $f(x, y)$ only relates to local parameters in the entire volume, our frequency learning scheme computes a single position in $f(x, y)$ from the entire phasor volume through Fourier transform. Full numerical integration (NI) of the Fourier transform (i.e., Eq. 1) requires computing an inner product between the entire phasor volume and the position-encoded volume $\exp\{j2\pi(ux + vy)\}$ [47, 59], prohibitively expensive for any practical frequency learning scheme. To make the computational tractable, we observe that if all input coordinates are equally spaced, then the Fourier transform simplifies to the Discrete Fourier Transform (DFT) that can be explicitly evaluated using fast Fourier transform (FFT) methods, e.g., the Cooley–Tukey algorithm [6]. To compute an arbitrary (off-grid) input coordinate (x, y) , one possible solution is to first compute a map of equally-spaced coordinates $f(x^*, y^*)$ by 2D FFT and then perform bilinear interpolation from the 2D on-grid map given. However, such a scheme, i.e., computing an entire dense volume with many unused vertices, provides a poor trade-off between complexity and accuracy.

To tailor our dilated phasor volume, we instead employ both FFT and NI to achieve both high accuracy and low complexity. Specifically, we perform 1D FFT along the non-dilated axis u to obtain an intermediate map $\mathbf{P}_v[x^*, v] = \sum_{u=0}^M e^{j2\pi u \frac{x^*}{M}} \mathbf{P}[u, v]$, with $x^* = [0, 1, \dots, M-1]$. Afterwards, linear interpolation and a per-sample NI along the dilated axis are conducted. Formally,

$$f(x, y) \approx \underbrace{\sum_{v=0}^D e^{j2\pi v \frac{y}{N}} \underbrace{\langle \mathbf{P}_v[x^*, v] \rangle}_{\substack{\text{FFT+interpolation} \\ \text{Numerical integration}}} }_{\text{Numerical integration}} = \tilde{\mathcal{T}}_*(\mathbf{P}) \quad (5)$$

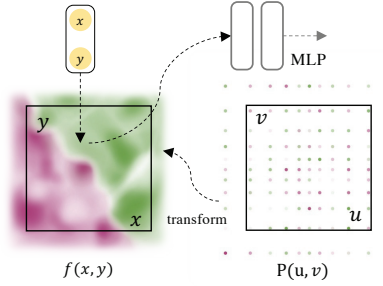


Figure 2: Pipeline of our PREF. The embedding field is translated from the dilated phasor grid via Fourier Transform.

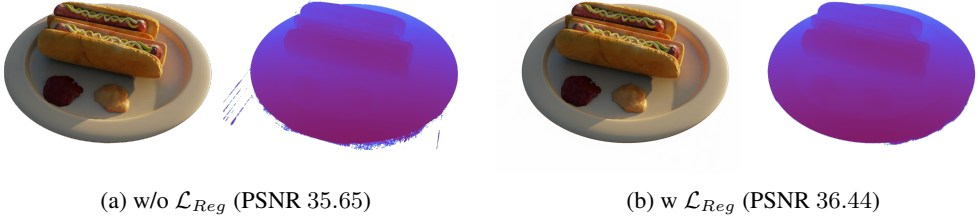


Figure 3: Effect of Parsvel regularizer on the hotdog scene from Synthetic-NeRF dataset [32]. Like most spatial embedding techniques, PREF alone without additional regularization can produce sinusoidal outliers - see the depth-map in Fig. (a). Imposing a Parsvel regularizer improves the overall quality, as shown in Fig. (b).

where $\langle \cdot \rangle$ is a linear interpolation operation that corresponds to interpolating $\mathbf{P}_v(x, v)$ from the intermediate map $\mathbf{P}_v[x^*, v]$. Note that, the length d in the dilated dimension is extremely small (details described in Sec. 4.1). Therefore, per-sample NI is very efficient, significantly reducing the training cost. Notice that $\tilde{\mathcal{T}}_*$ is an approximation to $\tilde{\mathcal{T}}$, convenient manipulations like differentiation in theorem 1 still apply but have approximation errors: the denser the intermediate map with FFT, the fewer the errors.

4.3 Volume Regularization

Many high dimensional signal reconstruction problems including NeRF are ill-posed. Therefore, PREF alone without additional priors may still produce reconstruction artifacts on such problems. In traditional signal processing, several regularization techniques such as the Lasso Regression (LR loss) and Total Variation regularizers (TV loss) have been imposed on natural signals to restrict the complexity (parsimony) of the reconstruction. Yet both LR and TV losses are designed for processing signals in the spatial domain and are not directly applicable to PREF. Noticing that Fourier transform preserves the energy of original quantity based on theorem 2, we therefore propose a novel Parseval regularizer as:

$$\begin{aligned} \mathcal{L}_{Reg}(\mathbf{P}) &= \|2\pi u \mathbf{P}[u, v]\|_2 + \|2\pi v \mathbf{P}[u, v]\|_2 \\ &= \sqrt{\sum_{u=0}^{N-1} \sum_{v=0}^{N-1} \|2\pi u \mathbf{P}[u, v]\|^2} + \sqrt{\sum_{u=0}^{N-1} \sum_{v=0}^{N-1} \|2\pi v \mathbf{P}[u, v]\|^2} \end{aligned} \quad (6)$$

The regularizer helps in suppressing high-frequencies directly during training. Lemma 3 illustrates that the Parseval regularizer equals the anisotropic TV regularizer in the spatial domain. A proof is included in the supplementary.

Lemma 3. *Let $f(x, y)$ be integrable, and $\mathbf{P}(u, v)$ be its Fourier transform. The anisotropic TV loss of $f(x, y)$ can be represented by $\|2\pi u \mathbf{P}(u, v)\|_2 + \|2\pi v \mathbf{P}(u, v)\|_2$.*

4.4 Complexity Analysis

Our PREF approximation scheme reduces the memory complexity by representing the feature space with a sparse set of frequencies, i.e., $O(kN^2D)$ to represent a k channel 3D feature volume. Similar to NGP, we can equip a shallow MLP module to PREF to achieve full spectral reconstruction.

Finally, to further improve efficiency, we adopt a two-step procedure for computing the PREF features for all input coordinates: (1) we conduct FFT to compute an off-grid intermediate map per batch of the input, and (2) we perform per sample numerical integration (NI) of the Fourier Transform. This indicates that the larger the batch, the lower the average complexity for the input samples. For a feature volume of size $O(k \times N^3)$ with X samples to be transformed and queried, our scheme reduces the complexity from $O(XkN^3)$ based on naive 3D NI to $O(kN^2 \log N + XkD^2)$ using 2D FFT and 1D

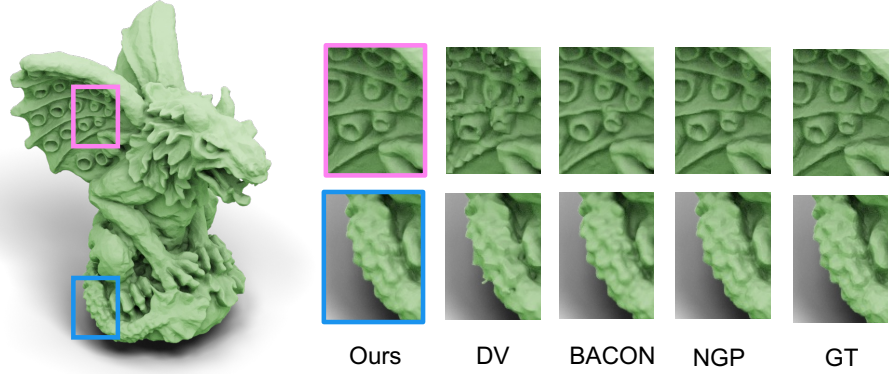


Figure 4: Quality visualization of regressed SDF. The left image shows our regressed model for Gargoyle. On the right, we compare our method to DV [45], BACON [24] and NGP [34].

Method	Memory (MB)	Armadillo		Gargoyle	
		IOU \uparrow	Chamfer- $L_1 \downarrow$	IOU \uparrow	Chamfer- $L_1 \downarrow$
PE [47]	6.0	96.65	1.21e-5	80.46	1.03e-4
BACON [24]	2.1	98.33	2.20e-6	98.76	3.65e-5
DV [45]	128.0	98.81	5.67e-6	97.99	1.19e-5
NGP [34]	46.7	99.34	5.54e-6	99.42	1.03e-5
Ours	36.0	99.02	5.57e-6	99.05	1.06e-5

Table 1: Quantitative results of SDF regression. We compare PREF with both coordinate-based models, PE [32] and BACON [24], and embedding-based models, Dense volume (DV) [45] and more advanced variant NGP [34].

NI. Notice that $X \gg N$ in a single training batch, so the overhead of FFT is moderate. In practice, our implementation only incurs 10% \sim 20% increase in computational cost over the spatially-embedded acceleration schemes. Yet PREF reduces the memory consumption, improves modeling/rendering quality via full spectral reconstruction, and provides convenient frequency manipulations.

5 Experiments

We evaluate our PREF on three neural reconstruction tasks, including image regression, SDF regression and radiance field reconstruction. The choice of phasor volume size and MLP varies with tasks, mainly for fair comparisons with the aforementioned baselines, which we detail in each task.

2D Image Regression and Reconstruction. 2D image regression aims to evaluate the capability of the representation supervised with all image pixels, and image reconstruction or image inpainting is trained with partial pixels and predicts the missing ones. We quantitatively evaluate the PSNR scores between the outputs and ground-truth images for both tasks.

We first conduct pilot experiments of frequency learning under the image regression task, as shown in Fig. 1. The dense grid setting, corresponding to the 3rd and the 5th column, adopts a linear interpolation in a learnable $8 \times 100 \times 100$ feature grid and optional, followed by an MLP; Our PREF uses the same volume resolution as the dense grids and performs the standard inverse Fourier transform to predict the target 512×512 image. Our method significantly outperforms the dense grid setting in terms of the convergence speed and the reconstruction quality of pixels. We owe this improvement to the periodic nature of our Fourier decomposition that globally regularizes the whole signal instead of regionally as that in dense grids. We show that the representation of local parameterization with linear interpolation can hurt its generalization ability, consequently producing noisy results and failing to reflect its high-order gradients.

	Natural	Text
Dense Grid	23.627 ± 4.137	27.446 ± 2.274
PE [47]	23.294 ± 3.245	26.852 ± 1.860
SIREN [43]	23.451 ± 3.414	26.808 ± 5.733
NGP [34]	24.137 ± 3.509	27.641 ± 1.852
Ours	24.208 ± 3.607	28.238 ± 2.371

Table 2: Image reconstruction results - PSNR (mean \pm standard deviation).

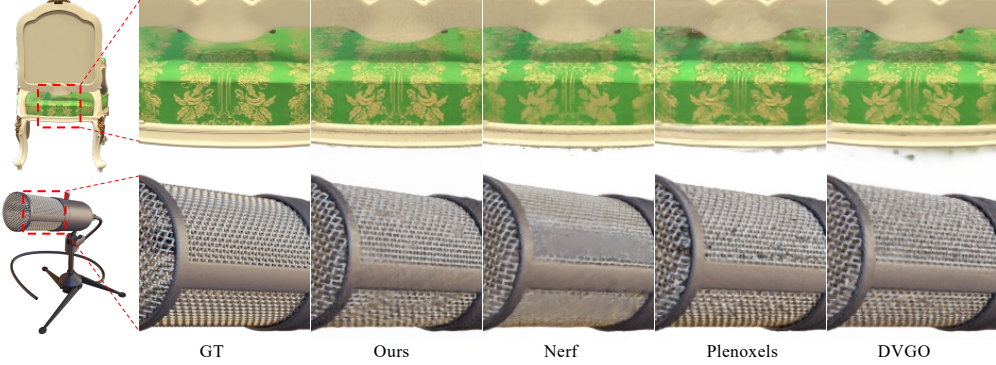


Figure 5: Quality results of our PREF and comparison methods (NeRF [28], Plenoxels [55] and DVGO [45]) on the synthetic NeRF scenes. Benefiting from our phasorial embedding, we manage to preserve details while rendering fewer outliers.

We further evaluate our PREF with the inpainting task, where we train our PREF with a regularly-spaced grid containing 75% missing pixels from each image in the Natural and Text dataset. In this experiment, our PREF consists of a phasorial volume with the reduced dimension $d = 8$ and a two-layer MLP. Following [11], We report test error on an unobserved 25% pixels in Tab. 2. Reasonably, our approach also achieves qualitatively better reconstruction results.

SDF regression and editing. Next, we explore the capability of PREF for geometric representation [30, 37] and editing. We evaluate the 3D shape regression from given point clouds together with its SDF values. We adopt Armadillo and Gargoyle, two widely-used models. For each model, we normalize the training mesh into a bounded box of $[-1, 1]$, and sample $= 2^{18}$ points for training: $4/8N$ points on the surface, $3/8N$ points around the surface by adding a Gaussian noise on the surface point with scale $= 0.01$, and $1/8N$ points uniformly sampled within the bounding box. We report the IOU of the ground truth mesh and the regressed signed distance field, by discretizing them into two 128^3 volumes. We also report the Chamfer distance metric by sampling $30k$ surface points from the predicted mesh with marching cube [26]. We implement DVGO by ourselves and adopt the implementation of NGP² for comparisons. We include detailed parameter choices in supplementary. The quantitative evaluation in Tab. 1 demonstrates that we achieve competitive results with existing SOTAs while remaining a more compact model. We also show the quality visualizations in Fig. 4. It shows that over-parameterization of DV leads to artifacts, while PREF reduces overfitting owing to its global representation where each position is synthesised with all spatial supports. NGP [34] also manages to recover details and reduce outliers, potentially owing to their compact and relatively global representation based on a multi-scale hashing function.

In line with recent frequency representation [24, 3], our trained SDF model also allows implicit surface editing [52] such as level of detail filtering. For example, we can apply a point-wise multiplication of a Gauss on the trained phasorial embedding to modulate the frequencies, as shown in Fig. 6. It could be useful for surface denoising, texture removal or multi-scale representation in the neural fields.

Neural Radiance Field Reconstruction. Finally, we evaluate PREF on the popular radiance field reconstruction tasks. NeRF reconstruction attempts to recover scene geometrics and appearance given a set of multi-view input images with posed cameras. In this task, we evaluate the reconstruction quality of the novel views and evaluate the model size for the compactness and the efficiency with its training speed. In practice, we individually model the density and color, then jointly optimize them via a volume render scheme [32] supervised only with image color. However, this sometimes leads to overfitting to the training view and leading to floaters in empty space due to the strong model capability. We utilize a Parseval regularization to regularize the embedding field, as described in Sec. 4.3. The Parseval regularizer helps reduce outliers and therefore improves the overall quality, as illustrated in Fig. 3. We set the expected volume size as 256^3 , roughly containing 36MB parameters. Please see supplementary for detailed information. During optimization, we apply a coarse-to-fine training scheme starting from the 128 low frequency series. We then progressively unlock the rest

²adopted from <https://github.com/ashawkey/torch-ngp>

Method	BatchSize	Steps	Time ↓	Size(MB) ↓	PSNR↑	SSIM↑
SRN [44]	-	-	>10h	-	22.26	0.846
NeRF [32]	4096	300k	~35h	5.0	31.01	0.947
SNeRG [14]	8192	250k	~15h	1771.5	30.38	0.950
NSVF [25]	8192	150k	>48h	-	31.75	0.950
PlenOctrees [56]	1024	200k	~15h	1976.3	31.71	0.958
Plenoxels [55]	5000	128k	11.4m	778.1	31.71	0.958
DVGO [45]	5000	30k	15.0m	612.1	31.95	0.957
NGP [34]	256k	30k	4.6m	87.3	32.63	0.921
TensoRF [7]	4096	30k	17.4m	71.8	33.14	0.963
Ours	4096	30k	18.1m	34.4	32.08	0.952

Table 3: Application for fast radiance fields reconstruction on the NeRF-synthetic dataset [32]. We compare our approach with both pure MLP models (SRN), positional encoding (NeRF, SNeRG, PlenOctrees) and dense volume based (Plenoxels, DVGO) approaches.

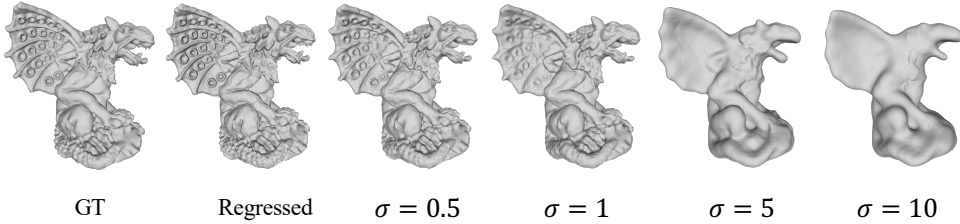


Figure 6: SDF editing via frequency modulation. This figure shows the smoothing effect, by point-wise scaling the embedding with a Gauss function, *i.e.*, $g(\mathbf{k}) = \exp(-\mathbf{k}^T \mathbf{k} \sigma^2)$, where \mathbf{k} is the frequency coordinate. Notice we perform smoothing in the neural fields, which is different to existing techniques like mesh smoothing.

high frequency series to be learnable at step [2000, 3000, 4000, 5500, 7000] to reach the expected frequencies 256. Tab. 3 shows the quantitative results; our model can be on par with the state-of-the-art radiance field reconstruction approaches while reaching compact modeling and a fast training process. A table on performance versus model size is also included in the supplementary.

6 Limitations

Speed-wise, PREF incurs additional training time caused by FFT but not in inference as it stores the transformed features. Consequently, it is slightly slower in training but comparably fast in inference to SOTA. As opposed to a global FFT that transforms the entire phasor volume, a local window-based FFT, also known as short-time FFT, may accelerate training and be potentially implemented on CUDA. Quality-wise, to maintain tiny volumes, PREF dilates along the reduced dimensions to cover the full spectra. As a result, it may introduce axis-biasing along the dilated ones, similar to [32]. To mitigate the problem, one may use NuFFT (Non-uniform Fast Fourier Transform) [12, 4, 33] to achieve non-uniform frequency sampling [47] as well as fast Fourier transform.

7 Conclusion

We have presented a novel neural approach for compact modeling that decompose a natural signal into Fourier series, and developed a fast and approximated transform scheme that efficiently synthesis spatial query with Fourier features for neural fields reconstruction. PREF produces high quality images, shapes, and radiance fields from given limited data and outperforms recent works. Benefiting from our physical meaningful Fourier decomposition and fast transformation, we allow explicitly manipulating the learned embedding under different frequencies. One interesting future direction is to apply our representation to efficient 3D-aware generative tasks, and PREF is potentially able to provide a more reasonable latent space, where low-frequency coefficients control structure and high-frequency coefficients control details.

References

- [1] M. Atzmon and Y. Lipman. Sal: Sign agnostic learning of shapes from raw data. In *IEEE/CVF Conference on Computer Vision and Pattern Recognition (CVPR)*, June 2020.
- [2] H. Bahouri, J.-Y. Chemin, and R. Danchin. *Fourier analysis and nonlinear partial differential equations*, volume 343. Springer, 2011.
- [3] J. T. Barron, B. Mildenhall, M. Tancik, P. Hedman, R. Martin-Brualla, and P. P. Srinivasan. Mip-nerf: A multiscale representation for anti-aliasing neural radiance fields. In *Proceedings of the IEEE/CVF International Conference on Computer Vision*, pages 5855–5864, 2021.
- [4] P. Beatty, D. Nishimura, and J. Pauly. Rapid gridding reconstruction with a minimal oversampling ratio. *IEEE Transactions on Medical Imaging*, 24(6):799–808, 2005.
- [5] R. N. Bracewell and R. N. Bracewell. *The Fourier transform and its applications*, volume 31999. McGraw-Hill New York, 1986.
- [6] E. O. Brigham. *The fast Fourier transform and its applications*. Prentice-Hall, Inc., 1988.
- [7] A. Chen, Z. Xu, A. Geiger, J. Yu, and H. Su. Tensorf: Tensorial radiance fields. *arXiv preprint arXiv:2203.09517*, 2022.
- [8] A. Chen, Z. Xu, F. Zhao, X. Zhang, F. Xiang, J. Yu, and H. Su. Mvsnerf: Fast generalizable radiance field reconstruction from multi-view stereo. In *Proceedings of the IEEE/CVF International Conference on Computer Vision*, pages 14124–14133, 2021.
- [9] W. Chen, X. Zhu, R. Sun, J. He, R. Li, X. Shen, and B. Yu. Tensor low-rank reconstruction for semantic segmentation. In *European Conference on Computer Vision*, pages 52–69. Springer, 2020.
- [10] Y. Chen, S. Liu, and X. Wang. Learning continuous image representation with local implicit image function. In *Proceedings of the IEEE/CVF Conference on Computer Vision and Pattern Recognition (CVPR)*, pages 8628–8638, June 2021.
- [11] R. Fathony, A. K. Sahu, D. Willmott, and J. Z. Kolter. Multiplicative filter networks. In *International Conference on Learning Representations*, 2020.
- [12] J. Fessler and B. Sutton. Nonuniform fast fourier transforms using min-max interpolation. *IEEE Transactions on Signal Processing*, 51(2):560–574, 2003.
- [13] A. Gropp, L. Yariv, N. Haim, M. Atzmon, and Y. Lipman. Implicit geometric regularization for learning shapes. In *International Conference on Machine Learning*, pages 3789–3799. PMLR, 2020.
- [14] P. Hedman, P. P. Srinivasan, B. Mildenhall, J. T. Barron, and P. Debevec. Baking neural radiance fields for real-time view synthesis. *arXiv preprint arXiv:2103.14645*, 2021.
- [15] Z. Huang, S. Bai, and J. Z. Kolter. Implicit²: Implicit layers for implicit representations. *Advances in Neural Information Processing Systems*, 34, 2021.
- [16] C. Jensen, R. Reed, R. Marks, M. El-Sharkawi, J.-B. Jung, R. Miyamoto, G. Anderson, and C. Eggen. Inversion of feedforward neural networks: algorithms and applications. *Proceedings of the IEEE*, 87(9):1536–1549, 1999.
- [17] M. Ji, J. Gall, H. Zheng, Y. Liu, and L. Fang. SurfaceNet: An end-to-end 3D neural network for multiview stereopsis. In *Proc. ICCV*, 2017.
- [18] T. Karras, M. Aittala, S. Laine, E. Härkönen, J. Hellsten, J. Lehtinen, and T. Aila. Alias-free generative adversarial networks. In *Proc. NeurIPS*, 2021.
- [19] T. Karras, S. Laine, and T. Aila. A style-based generator architecture for generative adversarial networks. In *Proceedings of the IEEE/CVF conference on computer vision and pattern recognition*, pages 4401–4410, 2019.
- [20] D. P. Kingma and J. Ba. Adam: A method for stochastic optimization. *arXiv preprint arXiv:1412.6980*, 2014.
- [21] M. Levoy and P. Hanrahan. Light field rendering. In *Proceedings of the 23rd annual conference on Computer graphics and interactive techniques*, pages 31–42. ACM, 1996.

[22] Z. Li, N. Kovachki, K. Azizzadenesheli, B. Liu, K. Bhattacharya, A. Stuart, and A. Anandkumar. Fourier neural operator for parametric partial differential equations. *arXiv preprint arXiv:2010.08895*, 2020.

[23] C.-H. Lin, W.-C. Ma, A. Torralba, and S. Lucey. Barf: Bundle-adjusting neural radiance fields. In *IEEE International Conference on Computer Vision (ICCV)*, 2021.

[24] D. B. Lindell, D. Van Veen, J. J. Park, and G. Wetzstein. Bacon: Band-limited coordinate networks for multiscale scene representation. In *Proceedings of the IEEE/CVF Conference on Computer Vision and Pattern Recognition*, pages 16252–16262, 2022.

[25] L. Liu, J. Gu, K. Z. Lin, T.-S. Chua, and C. Theobalt. Neural sparse voxel fields. *arXiv preprint arXiv:2007.11571*, 2020.

[26] W. E. Lorensen and H. E. Cline. Marching cubes: A high resolution 3d surface construction algorithm. *SIGGRAPH Computer Graphics*, 21(4):163–169, 1987.

[27] J. N. Martel, D. B. Lindell, C. Z. Lin, E. R. Chan, M. Monteiro, and G. Wetzstein. Acorn: Adaptive coordinate networks for neural scene representation. *arXiv preprint arXiv:2105.02788*, 2021.

[28] R. Martin-Brualla, N. Radwan, M. S. Sajjadi, J. T. Barron, A. Dosovitskiy, and D. Duckworth. Nerf in the wild: Neural radiance fields for unconstrained photo collections. In *Proceedings of the IEEE/CVF Conference on Computer Vision and Pattern Recognition*, pages 7210–7219, 2021.

[29] Q. Meng, A. Chen, H. Luo, M. Wu, H. Su, L. Xu, X. He, and J. Yu. Gnerf: Gan-based neural radiance field without posed camera. In *Proceedings of the IEEE/CVF International Conference on Computer Vision*, pages 6351–6361, 2021.

[30] L. Mescheder, M. Oechsle, M. Niemeyer, S. Nowozin, and A. Geiger. Occupancy networks: Learning 3d reconstruction in function space. *Proc. CVPR*, 2019.

[31] B. Mildenhall, P. P. Srinivasan, R. Ortiz-Cayon, N. K. Kalantari, R. Ramamoorthi, R. Ng, and A. Kar. Local light field fusion: Practical view synthesis with prescriptive sampling guidelines. *ACM Transactions on Graphics (TOG)*, 38(4):1–14, 2019.

[32] B. Mildenhall, P. P. Srinivasan, M. Tancik, J. T. Barron, R. Ramamoorthi, and R. Ng. Nerf: Representing scenes as neural radiance fields for view synthesis. In *European conference on computer vision*, pages 405–421. Springer, 2020.

[33] M. J. Muckley, R. Stern, T. Murrell, and F. Knoll. TorchKbNufft: A high-level, hardware-agnostic non-uniform fast Fourier transform. In *ISMRM Workshop on Data Sampling & Image Reconstruction*, 2020. Source code available at <https://github.com/mmuckley/torchkbnufft>.

[34] T. Müller, A. Evans, C. Schied, and A. Keller. Instant neural graphics primitives with a multiresolution hash encoding. *arXiv preprint arXiv:2201.05989*, 2022.

[35] M. Niemeyer, L. Mescheder, M. Oechsle, and A. Geiger. Differentiable volumetric rendering: Learning implicit 3d representations without 3d supervision. In *Proc. IEEE Conf. on Computer Vision and Pattern Recognition (CVPR)*, 2020.

[36] M. Oechsle, S. Peng, and A. Geiger. Unisurf: Unifying neural implicit surfaces and radiance fields for multi-view reconstruction. *arXiv preprint arXiv:2104.10078*, 2021.

[37] J. J. Park, P. Florence, J. Straub, R. Newcombe, and S. Lovegrove. Deepsdf: Learning continuous signed distance functions for shape representation. In *Proceedings of the IEEE/CVF Conference on Computer Vision and Pattern Recognition*, pages 165–174, 2019.

[38] K. Park, U. Sinha, J. T. Barron, S. Bouaziz, D. B. Goldman, S. M. Seitz, and R. Martin-Brualla. Nerfies: Deformable neural radiance fields. In *Proceedings of the IEEE/CVF International Conference on Computer Vision*, pages 5865–5874, 2021.

[39] S. Peng, M. Niemeyer, L. Mescheder, M. Pollefeys, and A. Geiger. Convolutional occupancy networks. In *European Conference on Computer Vision*, pages 523–540. Springer, 2020.

[40] C. R. Qi, H. Su, M. Nießner, A. Dai, M. Yan, and L. J. Guibas. Volumetric and multi-view cnns for object classification on 3d data. In *Proc. CVPR*, 2016.

[41] C. Reiser, S. Peng, Y. Liao, and A. Geiger. Kilonerf: Speeding up neural radiance fields with thousands of tiny mlps. *arXiv preprint arXiv:2103.13744*, 2021.

[42] A. A. Rusu, D. Rao, J. Sygnowski, O. Vinyals, R. Pascanu, S. Osindero, and R. Hadsell. Meta-learning with latent embedding optimization. *arXiv preprint arXiv:1807.05960*, 2018.

[43] V. Sitzmann, J. N. Martel, A. W. Bergman, D. B. Lindell, and G. Wetzstein. Implicit neural representations with periodic activation functions. In *arXiv*, 2020.

[44] V. Sitzmann, M. Zollhöfer, and G. Wetzstein. Scene representation networks: Continuous 3d-structure-aware neural scene representations. *arXiv preprint arXiv:1906.01618*, 2019.

[45] C. Sun, M. Sun, and H.-T. Chen. Direct voxel grid optimization: Super-fast convergence for radiance fields reconstruction. *arXiv preprint arXiv:2111.11215*, 2021.

[46] T. Takikawa, J. Litalien, K. Yin, K. Kreis, C. Loop, D. Nowrouzezahrai, A. Jacobson, M. McGuire, and S. Fidler. Neural geometric level of detail: Real-time rendering with implicit 3d shapes. In *Proceedings of the IEEE/CVF Conference on Computer Vision and Pattern Recognition*, pages 11358–11367, 2021.

[47] M. Tancik, P. P. Srinivasan, B. Mildenhall, S. Fridovich-Keil, N. Raghavan, U. Singhal, R. Ramamoorthi, J. T. Barron, and R. Ng. Fourier features let networks learn high frequency functions in low dimensional domains. *NeurIPS*, 2020.

[48] P. Wang, L. Liu, Y. Liu, C. Theobalt, T. Komura, and W. Wang. Neus: Learning neural implicit surfaces by volume rendering for multi-view reconstruction. *arXiv preprint arXiv:2106.10689*, 2021.

[49] P.-S. Wang, Y. Liu, Y.-Q. Yang, and X. Tong. Spline positional encoding for learning 3d implicit signed distance fields. *arXiv preprint arXiv:2106.01553*, 2021.

[50] D. N. Wood, D. I. Azuma, K. Aldinger, B. Curless, T. Duchamp, D. H. Salesin, and W. Stuetzle. Surface light fields for 3d photography. In *Proceedings of the 27th annual conference on Computer graphics and interactive techniques*, pages 287–296. ACM Press/Addison-Wesley Publishing Co., 2000.

[51] W. Xia, Y. Zhang, Y. Yang, J.-H. Xue, B. Zhou, and M.-H. Yang. Gan inversion: A survey. *arXiv preprint arXiv:2101.05278*, 2021.

[52] G. Yang, S. Belongie, B. Hariharan, and V. Koltun. Geometry processing with neural fields. *Advances in Neural Information Processing Systems*, 34:22483–22497, 2021.

[53] L. Yariv, J. Gu, Y. Kasten, and Y. Lipman. Volume rendering of neural implicit surfaces. In *Thirty-Fifth Conference on Neural Information Processing Systems*, 2021.

[54] L. Yariv, Y. Kasten, D. Moran, M. Galun, M. Atzmon, B. Ronen, and Y. Lipman. Multiview neural surface reconstruction by disentangling geometry and appearance. In *Proc. NeurIPS*, 2020.

[55] A. Yu, S. Fridovich-Keil, M. Tancik, Q. Chen, B. Recht, and A. Kanazawa. Plenoxels: Radiance fields without neural networks. *arXiv preprint arXiv:2112.05131*, 2021.

[56] A. Yu, R. Li, M. Tancik, H. Li, R. Ng, and A. Kanazawa. Plenotrees for real-time rendering of neural radiance fields. *arXiv preprint arXiv:2103.14024*, 2021.

[57] H. Yu, A. Chen, X. Chen, L. Xu, Z. Shao, and J. Yu. Anisotropic fourier features for neural image-based rendering and relighting. In *Proceedings of the AAAI Conference on Artificial Intelligence*, 2022.

[58] K. Zhang, G. Riegler, N. Snavely, and V. Koltun. Nerf++: Analyzing and improving neural radiance fields. *arXiv preprint arXiv:2010.07492*, 2020.

[59] E. D. Zhong, T. Bepler, B. Berger, and J. H. Davis. Cryodrgn: reconstruction of heterogeneous cryo-em structures using neural networks. *Nature methods*, 18(2):176–185, 2021.

-Supplementary-

A Phasorial Embedding Fields Implementation Details

Dilated Phasor Volume. Recall that PREF is a continuous embedding field corresponding to a multi-channel multi-dimensional square Fourier volume. We elaborate on implementation details. Let $\mathbf{P}[u, v, w]$ be a 3D phasor volume representing an embedding field $f(x, y, z)$.

Note that the $\mathbf{P}[u, v, w]$ is Hermitian symmetric when the $f(x, y, z)$ is a real-valued feature embedding, *i.e.*, $\mathbf{P}[u, v, w] = \mathbf{P}^*[-u, -v, -w]$ (*i.e.*, its complex conjugate). Further, based on the observation that natural signals are generally band-limited, we model their corresponding fields with band-limited phasor volumes $\mathbf{P}[u, v, w]$ where we are able to partially mask out some entries and factor the volume along respective dimensions, as shown in Fig 7. Thus we factorize the full spectrum into tri-thin embeddings by reusing the linearity of the Fourier Transform, $f(x, y, z) = \tilde{\mathcal{T}}(\mathbf{P}_u) + \tilde{\mathcal{T}}(\mathbf{P}_v) + \tilde{\mathcal{T}}(\mathbf{P}_w)$.

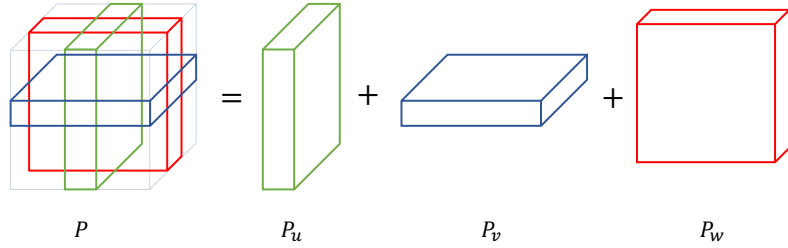


Figure 7: Phasor volume decomposition. Let the phasor volume with zero frequency centered. We selectively mask out some entries of the phasor volume as zero, then approximate the spatial feature embedding of a large phasor volume in terms of the sum of the embedding from three smaller ones, one for each dimension. The complete phasor volume to spatial feature embeddings is shown in the PyTorch pseudo-code in Algorithm 1.

IFT Implementation. Recall that for a 3D phasor volume, we approximate $\tilde{\mathcal{T}}$ via sub-procedures of applying 2D Fast Fourier Transforms (FFTs) and 1D numerical integration (NI) to achieve high efficiency. Therefore, given a batch of spatial coordinates, our PREF representation transforms them into a batch of feature embeddings in parallel where PREF can serve as a plug-and-play module. Such a module can be applied to many existing implicit neural representations to conduct task-specific neural field reconstructions. We present a sketchy PyTorch pseudo-code in Algorithm 1.

Phasor Volume Initialization. Our PREF approach can be alternatively viewed as a frequency space learning scheme to existing spatial coordinate-based MLPs. In our experiments, we found zero initialization works well for applications ranging from 2D image regression to 5D radiance fields reconstruction while certain applications require more tailored initialization, *e.g.*, geometric initialization in [1, 54]. This is because $\mathbf{P}(k)$ (*with k being the frequency coordinate*) needs to satisfy the unique constraints of $f(x)$. We thus initialize the phasor volume as follows: Let $f^\circ(x)$ be the initialization of $f(x)$. We have $\mathbf{P}^\circ(k) = \mathcal{T}(f^\circ(x))$, with \mathcal{T} as the Fourier transform. We then transform $\mathbf{P}^\circ(k)$ via the inverse Fourier transform $\tilde{\mathcal{T}}$ (*due to duality between $f(x)$ and $\mathbf{P}(k)$*) as the *approximation* to $f^\circ(x)$. We found such a strategy enhances stability and efficiency.

Computation Time. One of the key benefits of PREF is its efficiency. As discussed in Sec. 4.4, we conduct frequency-based neural field reconstruction by employing IFT, which is computationally low cost and at the same time effective. When the input batch is sufficiently large (*e.g.*, 4096×1024 samples per batch in radiance field reconstruction), the per-sample numerical evaluation will dominate the computational cost. Since such per-sample evaluation can be efficiently implemented using matrix product, it is essentially equivalent to adding a tiny linear layer. The overall implementation makes PREF nearly as fast as the state-of-the-art, *e.g.*, instant-NGP for NeRF. For example, on the Lego example, our PyTorch PREF produces the final result in 16 minutes on a single RTX3090, considerably

Algorithm 1: PyTorch pseudo code for PREF

```
class PREF(nn.Module):
    def __init__(self, res, d, ks):
        # res: resolution size
        # d: reduced dim size
        # ks: output kernel size
        Nx, Ny, Nz = res
        # log sampling freq in reduced dimension
        self.freq = torch.tensor([0]+[2**i for i in torch.arange(d-1)])
        self.Pu = nn.Parameter(torch.zeros(1, ks, d, Ny, Nz).to(torch.complex))
        self.Pv = nn.Parameter(torch.zeros(1, ks, Nx, d, Nz).to(torch.complex))
        self.Pw = nn.Parameter(torch.zeros(1, ks, Nx, Ny, d).to(torch.complex))
    def forward(self, xyz):
        # 2D Fast Fourier Transform
        Pu = torch.fft.ifftn(self.Pu, dim=(3,4))
        Pv = torch.fft.ifftn(self.Pv, dim=(2,4))
        Pw = torch.fft.ifftn(self.Pw, dim=(2,3))
        # 2D Linear interpolation
        xs, ys, zs = xyz.chunk(3, dim=-1)
        Px = grid_sample_cmplx(Pu.transpose(3,3).flatten(1,2), torch.stack([zs, ys], dim=-1)[None]).reshape(Pu.shape[1], Pu.shape[2], -1)
        Py = grid_sample_cmplx(Pv.transpose(2,3).flatten(1,2), torch.stack([zs, xs], dim=-1)[None]).reshape(Pv.shape[1], Pv.shape[3], -1)
        Pz = grid_sample_cmplx(Pw.transpose(2,4).flatten(1,2), torch.stack([xs, ys], dim=-1)[None]).reshape(Pw.shape[1], Pw.shape[4], -1)
        # 1D Numerical Integration
        fx = batch_NI(Px, xs, self.freq)
        fy = batch_NI(Py, ys, self.freq)
        fz = batch_NI(Pz, zs, self.freq)
        # Summation
        return fx+fy+fz
```

faster than the original NeRF and comparable to the PyTorch implementation of NGP. We are in the process of implementing PREF on CUDA analogous, and hopefully, it may achieve comparable performance to the CUDA version of NGP.

B Application to Image Regression

B.1 Implementation & Reproducibility Details

Pilot experiments. Before proceeding to more sophisticated tasks such as generation and reconstruction, we first explore a toy example that utilizes PREF to continuously parametrize an image, e.g., a 512×512 grayscale image. To better provide insights into our frequency-based learning framework, we use a 100×100 complex-valued grid to regress (upsample) the 512×512 input image via inverse Fourier transform, using PREF vs. bilinear upsampling on the same MLP network. From a signal processing perspective, if the image is band-limited, e.g., Nyquist frequency is the fold of 128, a frequency scheme should perfectly reconstruct the 512×512 image. Yet Bilinear interpolation exhibits aliasing due to the characteristics of the first- and second-order derivatives, as shown in the discussion and Fig. 1 in the paper. We then show the performance using embedding where we expand the grid size to a $8 \times 100 \times 100$ embedding volume followed by a three-layer MLP with a hidden dimension of 256 that maps the embeddings to pixels. Previous studies [43] have shown that improper activation functions can also lead to aliasing in high-order gradients, despite the choice of embedding techniques. Therefore, for comprehensive studies, we further compare various most-seen activation functions, including ReLU, Tanh, and the most recent, Sine [43]. Our experiments show that such a frequency-learning scheme consistently outperforms its spatial counterparts, potentially owing to its well-behaved derivatives and continuous nature, as shown in the line plot of Fig. 1.

Image completion. Next, we demonstrate PREF on image completion tasks. We use the commonly adopted setting [15, 11]: given 25% pixels of an image, we set out to predict another 25% pixels. We evaluate PREF vs. SATO on two benchmark datasets - Nature and Text. Specifically, we compare

PREF with a dense grid counterpart, and two state-of-the-art coordinate-based MLPs[28, 43]. The dense grid uses a $8 \times 100 \times 100$ resolution whereas PREF uses two 20×9 grids that correspond to the highest frequency of $2^7 = 128$. The two embedding techniques above use the same MLP with three linear layers, 256 hidden dimensions, and ReLU activation. We use Positional Encoding (PE) which consists of a 5-layer MLP with 7 frequencies encoding. We adopt SIREN from [43] that uses a 4-layer MLP and sine activation. Detailed comparisons are listed in Tab. 2.

Optimization details. All experiments use the same training configuration. Specifically, we adopt the Adam optimizer [20] with default parameters ($\beta_1 = 0.9, \beta_2 = 0.999, \epsilon = 1e^{-8}$), a learning rate of $1e^{-4}$. We use L_1 loss with $15k$ iterations to produce the final results.

C Application to Signed Distance Field Reconstruction

C.1 Task description

Next, we conduct the more challenging task of signed distance field (SDF) reconstruction. An SDF describes the shape in terms of a function as:

$$f(x) = \begin{cases} d(x, \partial\Omega), & \text{if } x \in \Omega^+ \\ -d(x, \partial\Omega), & \text{if } x \in \Omega^- \end{cases} \quad (7)$$

where $\partial\Omega$ is a closed surface and Ω^+ and Ω^- correspond to regions outside of and inside the surface respectively. d is the Euclidean distance from a point to the surface. Our goal is to recover a continuous SDF $f(x)$ given a set of discretized samples x^* of value $f(x^*)$ that commonly refers to samples from a mesh.

C.2 Implementation & Reproducibility Details

Data preparation. We adopt two widely used models: gargoyle (50k vertices) and armadillo (49k vertices). For each training epoch, we scale the model within a bounding box of $[-1, 1]$ and samples $N = 2^{18}$ points for training: $4/8N$ points on the surface, $3/8N$ points around the surface by adding Gaussian noise to the surface point with $scale = 0.01$, and the last $1/8N$ points uniformly sampled within the bounding box.

Metric. We report the IOU of the ground truth mesh and the regressed signed distance field by discretizing them into two 128^3 volumes. We report the Chamfer distance metric by sampling 30k surface points from the extracted mesh using the marching cube technique [26].

Baseline implementation details. For the embedding-based baselines, we use our implementation of the dense volume technique [45]. It contains $16 \times 128 \times 128 \times 128$ learnable parameters that transform the input coordinates to their feature embedding at a length 16 by trilinear-interpolation. We adopted the PyTorch implementation of NGP [34] from torch-ngp³, where they maintain a multi-level hash function to transform the spatial coordinate into feature embedding. We use a 16 num-of-level hash function with dimension 2. Consequently, the output feature embedding is of length 32. Please refer to [34] for more details on the implementation of multi-level hash. For our PREF, we use three $16 \times 128 \times 128 \times 6$ complex-valued volumes to nonlinearly transform the spatial coordinates to a 16d feature embeddings. All the embedding-based baselines and our PREF adopt the same MLP structure for fairness that consists of 3 layers that progressively map the input embedding to the 64 dimension features as well as to a scalar, with ReLU as the intermediate activation. Another baseline we compare against the positional encoding (PE) based NeRF that uses a wider and deeper coordinate-based MLP [32] where we encode the input coordinates into six frequencies in PE and use an MLP of 8 linear layers, 512 hidden dimensions, and ReLU activation. Tab. 1 lists individual model size and performance of the baseline vs. PREF. Our method manage to be on par with the state-of-the-art NGP [34] with a compact model size, and outperform its spatial counterpart [45] and frequency-based proceedings. We owe the improvement of PREF to its globally continuous nature that either allows for preserving details.

Training details. We provide additional details on how we train the baseline. As aforementioned, in each epoch, we sample a batch size of $N = 2^{18}$ to regress the SDF values. The MAPE loss is used

³<https://github.com/ashawkey/torch-ngp>

	Chair	Drums	Ficus	Hotdog	Lego	Materials	Mic	Ship	Mean	Size (MB)↓
PlenOctrees [56]	34.66	25.37	30.79	36.79	32.95	29.76	33.97	29.62	31.71	1976.3
Plenoxels [55]	33.98	25.35	31.83	36.43	34.10	29.14	33.26	29.62	31.71	778.1
DVGO [45]	34.09	25.44	32.78	36.74	34.46	29.57	33.20	29.12	31.95	612.1
Ours	34.95	25.00	33.08	36.44	35.27	29.33	33.25	29.23	32.08	34.4

Table 4: PSNR results on each scene from the Synthetic-NeRF dataset [32]. We show the comparisons of the dense volume variants with our PREF (frequency-based scheme).

Highest Freq	Chair	Drums	Ficus	Hotdog	Lego	Materials	Mic	Ship	Mean	Size (MB)↓
256	34.95	25.00	33.08	36.44	35.27	29.33	33.25	29.23	32.08	34.40
128	33.29	24.64	32.70	36.04	33.77	29.37	31.87	27.75	31.18	9.84
64	31.54	23.82	30.43	35.25	30.56	28.82	31.22	27.08	29.83	2.28
32	30.11	22.59	27.77	34.07	27.39	27.65	30.48	25.79	28.23	0.76

Table 5: Ablation study of phasor volume size (related to the highest frequency). We report the PSNR of each scene, the mean PSRN and the corresponding mean model size. We train each scene *less than* 18 minutes using a pure PyTorch implementation on an RTX 3090, as discussed in the text.

for error back-propagation. To optimize the networks, we use the Adam optimizer, with $\beta_1 = 0.9$, $\beta_2 = 0.99$ and $\epsilon = 1e^{-5}$. We use an initial learning rate $1e^{-4}$ and reduce the learning rate to $1e^{-5}$ at the 10th epoch. We adopt a batch size of $N/100$ to optimize all baselines whereas for our method 20 epochs.

D Radiance Fields Reconstruction

D.1 Task description

For radiance field, we focus on rendering novel views from a set of images with known camera poses. Each rgb value in each pixel corresponds to a ray cast from the image plane. We adopt the volume rendering model [28]:

$$\hat{C}(r) = \sum_i^N T_i (1 - \exp(-\sigma_i \delta_i)) c_i, \text{ where } T_i = \exp\left(-\sum_{j=1}^{i-1} \sigma_j \delta_j\right) \quad (8)$$

where σ_i and c_i are corresponding density and color at location x_i , δ_i is the interval between adjacent samples. Then we optimize the rendered color with the ground truth color with \mathcal{L}_2 loss.

$$\mathcal{L}_{RGB} = \frac{1}{M} \sum_{i=0}^M \|C(r) - \hat{C}(r)\|^2. \quad (9)$$

D.2 Implementation & Reproducibility Details

PREF model setting. We describe how PREF models the density σ and the radiance c . We use three $16 \times 256 \times 256 \times 1$ phasor volume cascaded with a two-layer MLP with hidden dimension 64 and output dimension 1 for computing the density (a scalar). We then use Softplus to map the raw output to the positive-valued density. For the view-dependent radiance branch, we use a relatively large volume of $32 \times 256 \times 256 \times 1$ followed by a linear layer to output $27d$ feature embedding. To render view-dependent radiance, we follow the TensorRF pipeline [9]: we concatenate the result with the positional encoded view directions and feed them into a 2-layer MLP with 128d hidden dimension and a linear layer to map the feature to color with Sigmoid activation. All linear layers except the output layer use ReLU activation.

Rendering. To compare with SOTAs [55, 45, 9], we train each scene using $30k$ iterations with a batch size of 4096 rays. We adopt a progressive training scheme: from the highest frequency of 128 to 256. Specifically, we gradually unlock the higher frequencies at the training step [2000, 3000, 4000, 5500, 7000]. Accordingly, the number of samples per ray progressively increases

from about 384 to about 1024. This allows us to achieve more stable optimization by first covering the lower frequencies and later high-frequency details. During training, we maintain an alpha mask to skip empty space to avoid unnecessary evaluations.

Optimization. As mentioned in the paper, our PREF uses the Parsvel regularizer \mathcal{L}_{Reg} to avoid overfitting where our objective is set to $\mathcal{L} = \mathcal{L}_{RGB} + \lambda \mathcal{L}_{Reg}$ with $\lambda = 1e^{-2}$. Without regularization, PREF may overfit specific frequencies, as shown in Fig. 3. On the NeRF synthetic dataset, PREF converges on average 18 minutes with 30k iterations on a single RTX 3090, with an initial learning rate of 0.002 and gradually decayed by a factor of 10 during the training. The Adam optimizer uses $\beta_1 = 0.9$ and $\beta_2 = 0.99$ by default.

D.3 Additional results

We report the breakdown results of our PREF on the Synthetic-NeRF dataset in Tab. 4. To further evaluate the effectiveness of our frequency encoding, we report the performance in Tab. 5 under different model sizes (by varying the phasor volume size). Notice that PREF produces reasonable results (with a mean PSNR of 28.23) even when the model size is reduced to ultra-small (0.76 MB), a potential benefit for downstream generative tasks that require training thousands of scenes.

E Application to Shape Editing

E.1 Implementation details

Recall that the continuous embedding field of PREF is synthesized from a phasor volume under various frequencies. Therefore, thanks to Fourier transforms, various tools such as convolution in the continuous embedding fields can be conveniently and efficiently implemented as multiplications. This is therefore a unique advantage of PREF compared with its spatial embedding alternatives [9, 45, 55, 34].

Let $\mathcal{M}(\cdot; \theta)$ and $\mathbf{P}[u, v, w]$ be the optimized MLP and phasor volume, respectively. $\tilde{\mathcal{T}}$ represents the inverse Fourier Transform. Recall that we obtain a reconstruction field by $\Phi(\mathbf{x}) = \mathcal{M}(\tilde{\mathcal{T}}(\mathbf{P}; \mathbf{x}); \theta)$. Modification to the original signal via convolution based filtering can now be derived as:

$$\Phi^*(\mathbf{x}) = \mathcal{M}(\tilde{\mathcal{T}}(\mathbf{P} \circ \mathbf{G}; \mathbf{x}); \theta) \quad (10)$$

where \circ denotes element-wise multiplication and $\mathbf{G} \in \mathbb{C}^{l \times N^3}$ is a filter.

Now, we explore how to manipulate $\Phi(\mathbf{x})$ via the optimized phasor volume \mathbf{P} and kernel \mathbf{G} . For simplicity, we only the Gaussian filter \mathbf{G} while more sophisticated filters can also be applied in the same. Assume

$$G(\mathbf{k}) = \exp(-\mathbf{k}^T \mathbf{k} \sigma^2), \quad (11)$$

where $\mathbf{k} = [u/N, v/N, w/N]$ and \mathbf{G} covers the complete frequency span of \mathbf{P} ; that is, we can scale the magnitude of phasor features frequency-wise. For example, by varying the Gaussian kernel size using σ , PREF can denoise the neural representation of the signal at different scales, as shown in Fig. 6.

F Parsvel Regularization

Lemma 4. *Let $f(x, y)$ be integrable, and $\mathbf{P}(u, v)$ be its Fourier transform. The anisotropic TV loss of $f(x, y)$ can be represented by $\|2\pi u \mathbf{P}(u, v)\|_2 + \|2\pi v \mathbf{P}(u, v)\|_2$.*

Proof: Recall the TV loss can be computed as $\|\nabla_x f(x, y)\|_2 + \|\nabla_y f(x, y)\|_2$. Since $f(x, y)$ and $\mathbf{P}(u, v)$ are Fourier pairs, we have Fourier transform preserves the energy of original quantity based on Parseval's theorem (theorem 2), *i.e.*,

$$\iint \|f(x, y)\|^2 dx dy = \sum_{u=0}^{M-1} \sum_{v=0}^{N-1} \|P(u, v)\|^2 du dv. \quad (12)$$

According to theorem 1, $\nabla_x f(x)$ and $j2\pi u P(u, v)$ are also Fourier pairs. The integration derivative along axis x is defined as,

$$\iint \|\nabla_x f(x, y)\|^2 dx dy = \sum_{u=0}^{M-1} \sum_{v=0}^{N-1} \|j2\pi u P(u, v)\|^2 du dv. \quad (13)$$

By taking square root on both sides, we have $\|\nabla_x f(x, y)\|_2 = \|2\pi u P(u, v)\|_2$. And $\|\nabla_y f(x, y)\|_2 = \|2\pi v P(u, v)\|_2$ can be derived with similar proof.